Available online at www.sciencedirect.com
SCIENCE DIRECT
Journal of Colloid and Interface Science ●●● (●●●●) ●●●–●●●
Journal of Colloid and Interface Science
www.elsevier.com/locate/jcis

The geometry of primary drainage

W. Brent Lindquist *

Department of Applied Mathematics and Statistics, Stony Brook University, Stony Brook, NY 11794-3600, USA

Received 20 June 2005; accepted 17 September 2005

Abstract

We show that arc menisci configuration under primary drainage in capillary tube cross sections and, by extension, in throats in the void structure of rock and soil, can be understood in terms of the computational geometry theory of medial axis analysis. The solution for arc meniscus configuration is developed for cross sections of arbitrary, simply connected polygonal shape at both entry- and over-pressure values during primary drainage for arbitrary values of wetting angle. Using this solution technique, we have obtained highly accurate solutions of entry pressure arc meniscus radius for over 21,500 throats obtained from analysis of computed tomography images in a suite of 4 Fontainebleau core samples ranging from 7.5 to 22% porosity. We show that the ratio A/P, of throat area to throat perimeter, is an excellent predictor of entry pressure meniscus radius (and hence entry pressure) for primary drainage for real pores, while inscribed radius and area equivalent radius over-predict entry pressure meniscus radius by factors of 1.5–3, and are consequently poor predictors.

Keywords: Drainage; Capillary pressure; Entry condition; Meniscus curvature; Contact angle; Wetting film

1. Introduction

The pressure required to force a non-wetting fluid into a capillary tube (filled with wetting fluid) of arbitrary, constant, cross-sectional area is a function of the geometry of the system. Mayer and Stowe [1] and Princen [2] have shown that this function may be derived either by balancing work of displacement with change in surface free energy or, equivalently, by considering the forces required to maintain equilibrium. Assuming a piecewise smooth cross-sectional perimeter, the capillary pressure, P_C^e necessary to invoke piston-like entry of the non-wetting fluid (primary drainage) is given by

$$P_C^e = \frac{(\sigma_{\mathrm{NS}} - \sigma_{\mathrm{WS}})L_{\mathrm{NS}} + \sigma_{\mathrm{NW}}L_{\mathrm{NW}}}{A_N}, \qquad (1)$$

where σ, L, and A refer, respectively, to surface tension (surface free energy), interphase contact length, and area. The subscripts N, W, and S refer, respectively, to non-wetting, wetting, and solid phases. Thus, L_{NS} is the length of the cross section perimeter separating the non-wetting fluid from the solid (tube); L_{NW} is the length of the interface between the two fluids; and A_N is the cross-sectional area of the non-wetting fluid. These quantities are illustrated using Fig. 1, which shows a tube cross section after entry of the non-wetting fluid at the critical entry pressure. (Throughout this paper, we assume negligible gravity affects and that the non-wetting fluid invades the entire length of the capillary tube; i.e. the main terminal meniscus is far removed from the cross section of interest.) Using the force balance relation (Young equation),

$$\sigma_{\mathrm{NS}} - \sigma_{\mathrm{WS}} = \sigma_{\mathrm{NW}} \cos\theta, \qquad (2)$$

where θ is the contact angle (wetting angle) between the wetting fluid and the solid wall, (1) can be expressed as

$$P_C^e = \frac{\sigma_{\mathrm{NW}}L_{\mathrm{NS}}\cos\theta + \sigma_{\mathrm{NW}}L_{\mathrm{NW}}}{A_N}. \qquad (3)$$

As the fluids are (assumed to be) in equilibrium, each of the so-called arc menisci (AB, CD, and EF) which separates the non-wetting and wetting fluids must have identical radii of curvature. Therefore

$$L_{\mathrm{NW}} = 2r\sum_i \alpha_i, \qquad (4)$$

---

* Fax: +1 631 632 8490.
E-mail address: lindquis@ams.sunysb.edu.
URL: http://www.ams.sunysb.edu/~lindquis.

0021-9797/$ – see front matter © 2005 Elsevier Inc. All rights reserved.
doi:10.1016/j.jcis.2005.09.041

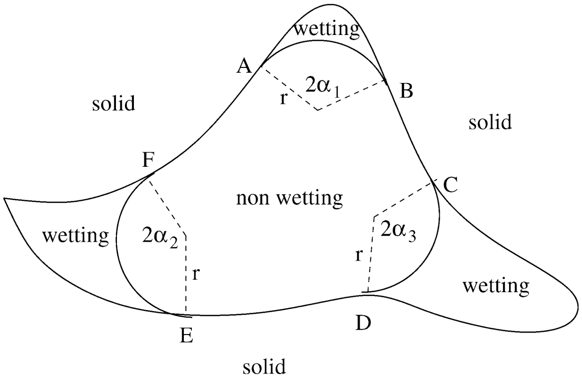

Fig. 1. Schematic of non-wetting fluid occupation of the cross section of a capillary tube of arbitrary, simply connected, cross-sectional shape.

where α_i is one half of the opening angle of arc meniscus i (Fig. 1). Further, at equilibrium the capillary pressure across each of the arc menisci is just P_C^e, which can be related to σ_{NW} by the Young–Laplace equation

$$P_C^e = \sigma_{\mathrm{NW}}/r. \tag{5}$$

Substituting (5) and (4) into (3) gives a non-linear equation,

$$2r^2\alpha + r\cos\theta L_{\mathrm{NS}}(r) - A_N(r) = 0, \tag{6}$$

to solve for the radius of curvature $r = r_{\mathrm{e}}$ of the arc menisci at the critical entry pressure. In (6), we have let $\alpha \equiv \sum_i \alpha_i$ and have also noted the implicit dependence of L_{NS} and A_N on r. It is through α, L_{NS}, and A_N that the geometry of the cross section determines the critical value, r_{e}. With r_{e} known, the critical entry pressure is then determined from (5).

We devote this article to a discussion of the solution of (6) for cross sections of *arbitrary, simply connected polygonal shape*. We note that the above description provides a model for penetration of a non-wetting fluid through the constriction (throat) separating two pores. This has become of primary importance in network models of two- (e.g. [3]) and three-phase (e.g. [4,5]) flow. In addition to providing entry pressure conditions, the solution quantifies details of the wetting fluid films occurring in corners. Such films provide critical pathways for wetting fluid movement and play important roles in trapping behavior (e.g. [6]).

Historically (6) was solved for special cross-sectional tube shapes [1,2,7–14]. With regard to network flow modeling, the significant solution was for irregularly shaped triangular tubes [15–17] and regular polygons [17–20]. Triangular and rectangular cross sections, as well as circular sections (which do not admit corners but can be contrived to model film flow), have since dominated network flow models. To quote Blunt [21], "It is difficult to represent every nook and cranny in the pore space directly. A simpler approach, adopted by many authors, is to assign some simple shape to the pore and throat cross sections that accommodates wetting layers. Just as in the assignment of effective pores sizes, there is no suggestion that the real pore space is represented by some idealized constant cross section—the shape is chosen simply to place the correct volume of wetting phase in layers in a pore whose center is filled by non-wetting phase and to give the right hydraulic conductivity to the layers."

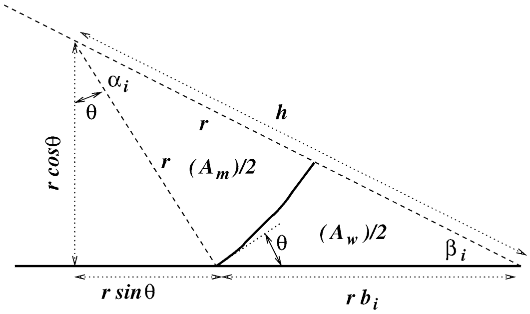

Fig. 2. Geometric quantities related to a stable meniscus, radius r, wetting angle θ, in a corner defined by a single convex vertex.

With the advent of synchrotron X-ray computed microtomography (CT) (e.g. [22]) and the development of image analysis software [23–27] to quantify cross-sectional pore and throat shapes of real rock samples at resolutions below 5 µm, it is clear that it is much more accurate to represent cross sections as irregular polygons. In this article we present a general solution method of (6) for irregular, simply connected polygons. The solution method is sufficiently rapid that computation of entry pressures for cross sections in an entire network model can be tabulated and referenced by the network model via look-up. However, approximation of cross-sectional shapes by simply geometric forms will continue to be utilized. We therefore also consider the accuracy of current approximations.

The geometry of an arc meniscus in a single (convex) corner of a polygon is amenable to straightforward analysis [3,28]. Exploiting the symmetry about the bisector of the angle, Fig. 2 displays the relevant geometry for a meniscus of radius r. Geometrical analysis gives relationships for the areas A_m and A_w, the relationship

$$b_i \equiv \frac{\cos(\theta + \beta_i)}{\sin\beta_i}, \tag{7}$$

and the important angular relation

$$\alpha_i = \pi/2 - \theta - \beta_i. \tag{8}$$

From (8) follows the condition

$$\theta + \beta_i \leqslant \pi/2, \tag{9}$$

which, for a given wetting angle θ, determines whether a convex vertex of half-angle β_i will contain an arc meniscus (and a wetting phase film).

With respect to approximations for throat cross-sectional shapes, effective cross-sectional radii from mercury porosimetry and distributions of throat areas from image analysis of CT scans are available from measurements on real rock samples. Using an approximate cross-sectional model based upon a regular polygon of fixed number, n, of vertices, either type of experimental value is sufficient to define a unique cross section. (It is common to use $n = 3$ or 4 in modern network models.) For a regular polygon, A_N depends quadratically on r, L_{NS} depends linearly on r, the solution of (6) is just the solution of a quadratic, the negative branch of the solution is physically meaningful, and the solution can be expressed as (see also [19])

$$\frac{r_{\mathrm{e}}}{P} = \frac{2G}{\cos\theta + [\cos^2\theta + 4G(\alpha - b\cos\theta)]^{1/2}}, \tag{10}$$

where α was defined above, $b \equiv \sum_i b_i$, and $G \equiv A/P^2$ is a dimensionless ratio of the polygon area A and perimeter P known as the shape factor [15]. Using the well known relations for a regular polygon of side length d,

$$\begin{aligned} &\beta_i = \beta = \pi/2 - \pi/n, \quad i = 1, \ldots, n, \\ &A = nd^2\tan(\beta)/4, \qquad P = nd, \end{aligned} \tag{11}$$

(10) can be simplified to

$$r_{\mathrm{e}} = \frac{A}{P}\left\{\frac{2}{\cos\theta + [\cot(\pi/n)(\pi/n - \theta + \sin\theta\cos\theta)]^{1/2}}\right\}. \tag{12}$$

As written, (10) can also be applied to irregular triangles [15,16] (and rectangles [11]) as long as $\sum_i$ in the definitions of α and b occur only for vertices having an arc meniscus (i.e. for vertices i such that $\theta + \beta_i \leqslant \pi/2$). It can also be extended to irregular polygons *as long as each arc meniscus in the solution corresponds to at most one polygon vertex* [17]. This condition, however, will not be true in general for solutions to (6) for non-triangular, irregular convex polygons, and will certainly fail for most non-convex polygons.

Recognition of the importance of G for regular, convex polygons, has prompted fitting network flow model cross sections to shape factor measurements [3,15,16].

2. Primary drainage, $\theta = 0$

Since [15] it has been recognized that, for a single vertex, the center of curvature of an arc meniscus in that corner must lie on the angular bisector of the vertex. Each point p on an angular bisector for a vertex v_i has the property that it is the center of an inscribed circle $r_i(p)$ which tangentially touches the two edges incident at v_i, where $0 \leqslant r_i(p) \leqslant r_{\mathrm{mic}}$. Exploiting the symmetry about the bisector in the case of an arc meniscus in a single corner (Fig. 2), allows the geometry to be computed in terms of half-angles, as reflected in the solutions (10) and (12). For a regular convex polygon, and for any irregular triangle, the angular bisectors meet at the center of mass. The center of mass is therefore the center c of a maximally inscribed circle, radius r_{mic}, which tangentially touches each edge.

In the computational geometry literature, these angular bisectors, extending from each vertex to the center of mass, comprise the *medial axis* (MA) of the interior of any regular convex polygon or irregular triangle. The concept of the MA is more general than these two restricted polygon types suggest [29]; for our purposes we concentrate on a discussion of the MA for the interior of any simply connected polygon having n vertices. As is customary in the computational geometry literature, the perimeter of the polygon shall be considered to consist of n ordered vertices, v_i, with an open line segment (edge) joining each pair v_i, v_{i+1} (with $v_{n+1} \equiv v_1$). Associated with each pair (edge–edge, edge–vertex, or vertex–vertex) of perimeter components is a bisector, a curve of points with the property that each point on the bisector is the center of an inscribed circle that tangentially touches a point on each component of the perimeter pair. (For open line segments, the point tangentially touched may be the terminating point of the closure of the line segment.) If a perimeter component is a vertex, we clarify that "tangentially touching" means that the inscribed circle passes through the vertex. Fig. 3 illustrates the bisectors for each type of perimeter component pair. For both an edge–edge and a vertex–vertex pair the bisector is a straight line, Figs. 3a, 3b. For a vertex–edge pair, the bisector is either a conic section, specifically a parabola, in the case in which the vertex is not coincident with a terminating point of the closure of the open edge segment, Fig. 3c, or a straight line, if the vertex is coincident with a terminating point of the closure of the open edge segment, Fig. 3d.

For a simply connected polygon composed of n vertices and n edges, there are $2n(2n-1)/2$ bisectors. A subset of size $O(n)$ of segments of these bisectors forms the edges of a Voronoi tessellation of the interior of the polygon relative to the perimeter components (i.e. each perimeter component $\mathcal{C}_i$ is in 1–1 correspondence with a Voronoi cell $\mathcal{V}_i$ of the tessellation) [30,31]. Each point in the interior of $\mathcal{V}_i$ is closer to component

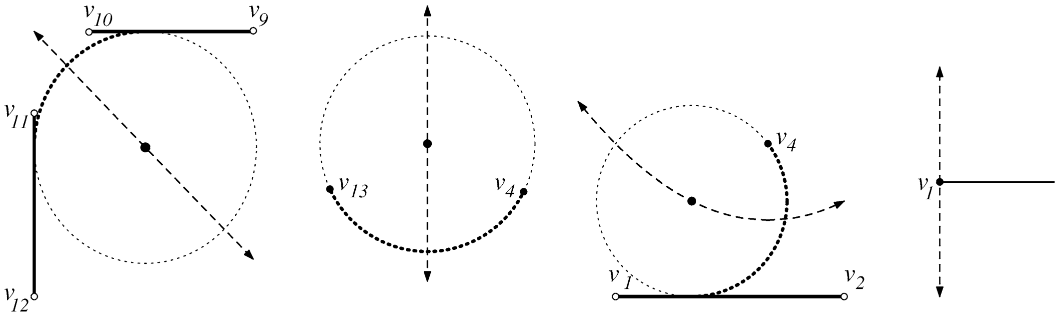

(a) (b) (c) (d)

Fig. 3. Illustrations of bisectors (dashed) for the three perimeter component pairs of a polygon: (a) edge–edge; (b) vertex–vertex; (c) vertex–edge (vertex not coincident with end-point of closure of open edge segment); (d) vertex–edge (vertex coincident with end-point of closure of open edge segment). Also highlighted is an example point on each bisector and the corresponding inscribed circle (dotted) which "tangentially touches" the perimeter components. The portion of each inscribed circle in the assumed centrifugal direction along the bisector has been darkened to illustrate the arc-meniscus between a non-wetting and a perfectly wetting ($\theta = 0$) fluid during drainage. (The remaining portion of each circle represents an arc-meniscus for a primary imbibition scenario in which the roles of (perfectly) wetting and non-wetting fluids are reversed.)

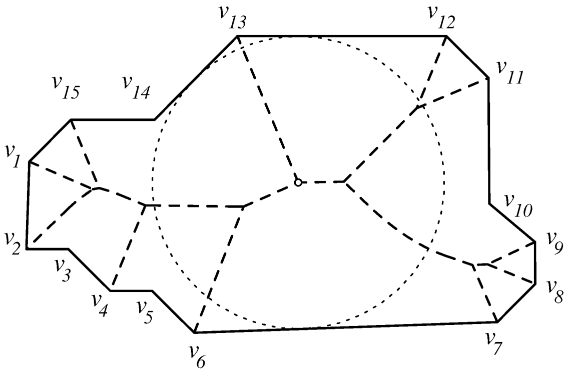

Fig. 4. The MA (dashed lines) of the interior of a polygon (solid lines). The light dotted curve shows a maximally inscribed circle of maximum possible radius r_{mic}. Its center location, on the MA, is the open point.

$\mathcal{C}_i$ than to any other perimeter component. The edges of this Voronoi tessellation form a tree structure. The MA for the interior of a simply connected polygon is a tree structure composed of all edges of the Voronoi tessellation excluding any tessellation edge of type (d) in Fig. 3. The type (d) Voronoi edges emanate from reflux (non-convex) vertices in the polygon interior. (Elimination of type (d) Voronoi edges merges Voronoi cells that are coincident at the reflux vertex.) As these type (d) edges are leaf edges of the Voronoi tree, their elimination leaves a MA which is also a tree. Fig. 4 shows the MA for an example polygon. As it is composed of segments of bisectors, each point on the interior MA is the center of some inscribed circle that tangentially touches at least two distinct points, each on a distinct perimeter component. (As bisectors can cross, a MA point may correspond to the crossing point of two or more bisectors—hence the inscribed circle centered at such a point may touch more than two perimeter points/components.) Conversely, as each MA point lies on some edge of a Voronoi tessellation, each point on a perimeter element is tangentially touched by an inscribed circle centered on some point on the interior MA. (This can be shown by enlarging a disk, initially of zero radius, within the interior of the polygon, making sure that the disk remains in tangential contact with the perimeter point in question. The center of this disk will eventually cross the MA.)

The following well-known properties of the MA for the interior of a polygon will be useful.

Property 0. *The MA is a tree structure formed from the union of segments of straight line and conic arc bisectors corresponding to perimeter component pairs. Conic arc sections of the tree correspond to segments of edge–vertex bisectors, where the vertex is a reflux* (*concave*) *vertex of the polygon; straight line sections correspond either to segments of edge–edge or vertex–vertex bisectors. An edge in the MA tree is a bisector segment of specific type* (*edge–edge, edge–vertex, vertex–vertex*). *Branch vertices in the tree are points common to bisector segments of two different types.* (*With bisectors of the form in Fig.* 3*d excluded from the MA, degree-*2 *branch vertices exist in the tree.*) *Leaf* (*degree-*1) *vertices terminate straight line segments; each leaf vertex of the tree is coincident with a vertex location on the polygon perimeter.*

Property 1. *Each point p of the MA can be assigned a unique distance value $r(p)$ which is the length of the radius of the inscribed circle centered at p which tangentially touches the two perimeter components to which the bisector containing p corresponds.*

Property 2. *The radius values $r(p)$ form a continuous function on the MA tree.*

Property 3. $0 \leqslant r(p) \leqslant r_{\max}$, *where the value of $r_{\max}$ is unique for a given polygon.*

Property 4. *If $r(p_0) = r_{\max}$, then p_0 may not be unique. However p_0 is either a branch point of the MA, or p_0 lies on a straight edge of the MA. In the latter case, $r(p) = r_{\max}$ for all points* (*including both terminating branch points of that edge*) *on the straight edge containing p_0.*

From Property 4, we can always root the MA tree at a tree vertex location p_0 having the property $r(p_0) = r_{\max} = r_{\mathrm{mic}}$. We therefore assume the MA tree is so rooted. Let p be a point on the MA. We define the *centripetal direction* from p as the (unique) direction along the MA toward the root, and the *centrifugal direction* from p as the (unique) direction along the MA away from the root (i.e. "toward some leaf"). We will also use centripetal in a colloquial sense to denote direction "toward the polygon interior" and centrifugal to denote direction "toward the polygon perimeter."

From the properties of the MA, the following theorem holds:

Theorem 1. *For a drainage displacement involving a perfectly wetting fluid* ($\theta = 0$), *the centers of curvature of arc-menisci separating the two fluids must lie on the interior MA of the polygon.*

Theorem 1 and Properties 0–4 provide the basis for solving (6) for the arc menisci radius and pressure at entry conditions, and for quantifying the movement of the arc menisci as capillary pressure increases above entry pressure. In Section 3 we will extend Theorem 1 to non-zero wetting angles.

We invoke the following assumption.

Assumption 1. We assume that the radius function $r(p)$ is a monotonically increasing function as one moves from any leaf ($r = 0$) to the root ($r = r_{\max}$) of the MA tree structure.

This assumption guarantees unique meniscus configuration solutions to (6) by precluding polygons whose perimeter shape would allow for the possibility of multiple solutions [1,14]. The purpose of this paper is to establish the geometrical connection between meniscus position and the medial axis. Allowing for non-monotonicity will not change this connection, rather it introduces an additional (combinatorial) problem of determining which of multiple meniscus combinations is an appropriate solution. At worst, many allowed combinatorial combinations will be valid solutions of (6) and a unique physical solution must be determined from conditions subsidiary to (6). We also note that, as the polygons we are most interested in studying are throats in a porous medium, this assumption will, almost always, be satisfied.

2.1. *Entry pressure meniscus configuration*

If (6) has a solution r_e for polygon P, then $0 \leqslant r_e \leqslant r_{mic}(P)$. If $r(p_1) \leqslant r_e \leqslant r(p_2)$ for a MA edge joining branch points p_1 and p_2 then an arc meniscus must be centered on this MA edge. As $0 \leqslant r(p) \leqslant r_{mic}$ monotonically on each leaf to root path in the MA tree structure, one such tree edge will be found for each leaf to root path in the tree. (The same tree edge/arc meniscus may however serve several leaf to root paths.)

A numerical algorithm can be constructed to solve (6) by performing a search in the function space $r(p)$ until a value of r is found such that evaluation of the LHS of (6) is zero (to within an acceptable tolerance). For each value of r investigated, a search over all tree edges will identify all points on the MA which are centers of arc menisci. As $0 \leqslant r_e \leqslant r_{mic}(P)$, the bisection search algorithm is a logical choice for the $r(p)$ search. The bisection search sequence $r_1, r_2, \ldots$ is begun with the two starting values $r_1 = 0 + \epsilon$, $r_2 = r_{mic} - \epsilon$ where ϵ is a small, positive tolerance to guard against floating point ambiguities in the numerical algorithm. For the ith value, r_i, in the bisection sequence, we find the unique point p_j on each appropriate branch j of the MA where $r(p_j) = r_i$. The centrifugal portion of the inscribed circle of radius r_i centered at p_j is the potential arc-meniscus for a solution with $r_e = r_i$. Fig. 5 shows the geometry based upon the polygon of Fig. 4 at a representative value of r_i. (In fact, a value r_i extremely close to r_e has been used for the figure.) From this geometry the LHS of (6) is evaluated. The open point is the vertex used as the root of the MA tree. p_j is the location of the point on the tree branch j having $r(p_j) = r_i$. The dashed arcs are the centrifugal segments of the respective inscribed circles centered at p_j (radius r_i) which would be fluid arc menisci for a solution to $r_e = r_i$. The area A_N required in (6) is the sum of the polygon area A_c (outlined by heavy solid lines) and the areas, $A_i, \ldots, A_6$, of the menisci defined arcs. The perimeter length L_{NS} in (6) is that portion of the boundary of the polygonal area A_c that overlaps with the original polygon perimeter. (Given the locations of the corners of the polygon of area A_c, these areas and perimeter lengths are straightforwardly computable.) With $A_N(r_i)$ and $L_{NS}(r_i)$ computed, the LHS of (6) is evaluated. The sign of the value of the LHS determines the value of r_{i+1} in the bisection search.

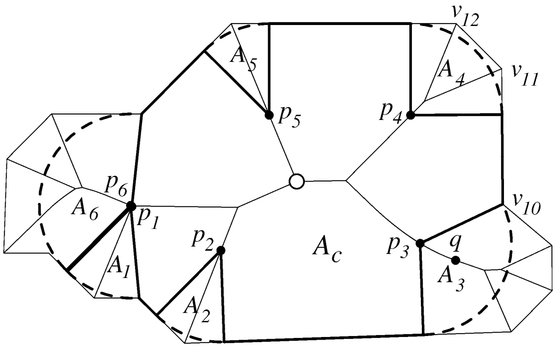

Fig. 5. Geometry for the evaluation of the LHS of (6) for a value $r = r_i$.

Of note in Fig. 5 is how close points p_i on separate branches of the MA approach one another during the bisection search algorithm if the value of r_i approaches a value appropriate for a branch point of the MA. (See points p_1 and p_6.) For such points, the corresponding inscribed circles also closely approach each other at one end. The numerical algorithm used for the bisection search must be sufficiently robust to detect and resolve such occurrences.

2.2. *Over-pressure in primary drainage*

After entry of the non-wetting fluid at P_C^e, if the capillary pressure P_C is further increased (quasi-statically), the (common) radius of the arc menisci deceases in accordance with (5). From the above discussion we see that the center points of the (decreasing radius) meniscus arcs move centrifugally along the MA branches. From Fig. 5 we immediately see the geometrical explanation for two well known phenomenon that occur in primary drainage.

From region A_4 (for example), we see that an arc meniscus will split as the meniscus center point passes a branch point on the MA tree. At the branch point, the meniscus comes into contact with a third perimeter edge component (edge $v_{11}v_{12}$ in Fig. 5) and the meniscus will bifurcate in two, each daughter meniscus moving toward a separate vertex of the polygon.

From region A_3, before any splitting can occur, the entry meniscus (initially centered at p_3) is pinned at its top end at vertex v_{10} as the meniscus center moves along the MA bisector segment containing p_3. As soon as the center moves from this vertex–edge bisector to the edge–edge bisector (at point q), the top end of the meniscus becomes unpinned. Although, no example is shown in Fig. 5, if the meniscus center is situated on a (straight) vertex–vertex bisector, the meniscus will remained pinned (at each end) at the two vertex points. *Thus pinning occurs whenever the meniscus center point is moving along either a vertex–edge or vertex–vertex bisector on the MA.*

It is important to re-emphasize that although discontinuity behavior (splitting) in the menisci occurs at branch points of the MA tree, the meniscus radius function $r(p)$ has no discontinuity through branch points of the tree.

We now slightly relax Assumption 1, to the case where the radius function $r(p)$ is a non-decreasing function as one moves centripetally on the MA tree structure. This allows $r(p)$ to be constant over an edge–edge bisector on the MA. This can only occur for edge–edge pairs on the perimeter of the polygon that are parallel to each other.) If such a MA segment occurs in the centrifugal direction from an entry pressure meniscus configuration, the meniscus will be metastable when its center lies on such a segment. The situation is illustrated in Fig. 6. As the function $r(p)$ is constant along the MA edge–edge bisector from p to q, when the arc meniscus center hits p at some overpressure P_C, the meniscus center is metastable, and will move immediately (spurt) to q with no change in the value of P_C. (The rate of movement will presumably be controlled by viscosity effects which determine how rapidly the wetting fluid can leave through the wetting films and the non-wetting fluid occupy the displaced region.)

As stated earlier, we do not bother to relax Assumption 1 completely, to allow for non-monotonic behavior of $r(p)$, since this introduces multiple meniscus configuration solutions. (This is equivalent to introducing "throating" behavior within the cross-sectional shape of the polygonal throats.)

3. Primary drainage, $\theta > 0$

With reference to Figs. 2 and 3, we see that, for $\theta > 0$, the center of an arc meniscus of radius r will be located a distance $r \cos\theta$ from a perimeter edge component, but must be located the full distance r from a perimeter vertex component. Thus, for $\theta > 0$, *an arc meniscus center will remain on the edge–edge and vertex–vertex bisectors shown in Figs. 3a, 3b, but must move off parabolic bisectors for vertex–edge components*. As illustrated in Fig. 7, the appropriate vertex–edge "bisector" for $\theta > 0$ is a hyperbola. In Fig. 7, the edge component is v_1v_2 and the vertex component is v_4. The edge component v_1v_2 becomes the conic directrix and the vertex v_4 is the focus for the hyperbola [32]. The eccentricity of the hyperbola is given by $e = 1/\cos\theta$. (These statements are also true for a $\theta = 0$ parabolic bisector.)

The arc meniscus centers now lie on a modification of the MA which consists of segments of edge–edge bisectors, vertex–vertex bisectors, and vertex–edge hyperbolic "bisectors." As this modified MA has not been studied in the computational geometry literature, we take the liberty of referring to it as the *drainage axis* (DA). As the DA changes with wetting angle, we shall designate this angle dependence through the functional notation DA(θ). Following convention, when the wetting angle is specified, we employ degrees rather than radians.

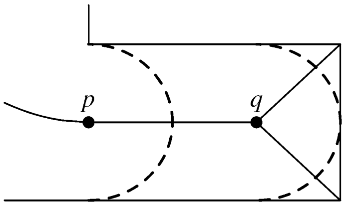

Fig. 6. A constant value for $r(p)$ on an edge–edge bisector leads to spurt motion (from p to q) of the arc meniscus center with no change in the radius of the arc meniscus.

Fig. 8 illustrates how these hyperbolic vertex–edge bisectors connect with other bisectors to form the DA. The left figure displays the v_4–v_1v_2 vertex–edge parabolic bisector (labeled h_0) and the v_1v_2–v_3v_4 edge–edge bisector (labeled $b_{12,34}$). The parabolic bisector touches the $b_{12,34}$ bisector tangentially at the point p_0. This is the point of attachment of the parabolic bisector to the $b_{12,34}$ bisector in the MA. The MA would consist of the segment of the parabolic bisector to the left of p_0, and the segment of $b_{12,34}$ to the right of p_0. The first derivative of the MA path is continuous across p_0.

Over a range of values $0 < \theta < \theta_{\max}$, each hyperbolic bisector (an example labeled h_θ is shown in Fig. 8) intersects the $b_{12,34}$ bisector at two points (labeled p_θ and p_θ^* in the figure). The point p_θ, which forms a centripetal angle of θ relative to edge v_3v_4 at vertex v_4 as indicated, is the point of attachment of the hyperbolic bisector to the $b_{12,34}$ bisector in the DA. The DA would consist of the segment of the hyperbolic bisector to the left of p_θ, and the segment of $b_{12,34}$ to the right of p_θ. The first derivative of the DA path is not continuous across p_θ. The point p_θ will move continuously to the left of p_0 along the $b_{12,34}$ bisector as θ is increased from 0.

As seen in Fig. 8 (left), there exists a maximum value, $\theta_{\max}$, above which the hyperbolic bisectors intersect $b_{12,\,34}$ only at

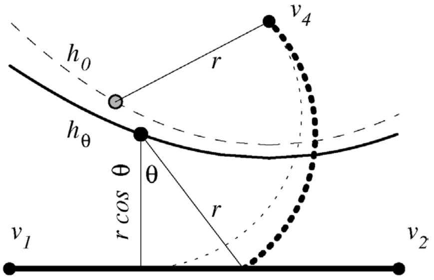

Fig. 7. Illustration of an arc meniscus between a perimeter edge v_1v_2 and a perimeter vertex v_4 for $\theta = 0$ (light dotted line) and $\theta = 36°$ (heavy dotted line). For $\theta = 0$ the meniscus center (lightly shaded point) follows the parabolic bisector (dashed curve labeled h_0) on the MA; for $\theta > 0$ the meniscus center (dark point) follows a hyperbolic conic section (solid curve labeled h_θ) displaced from the MA toward the perimeter edge component.

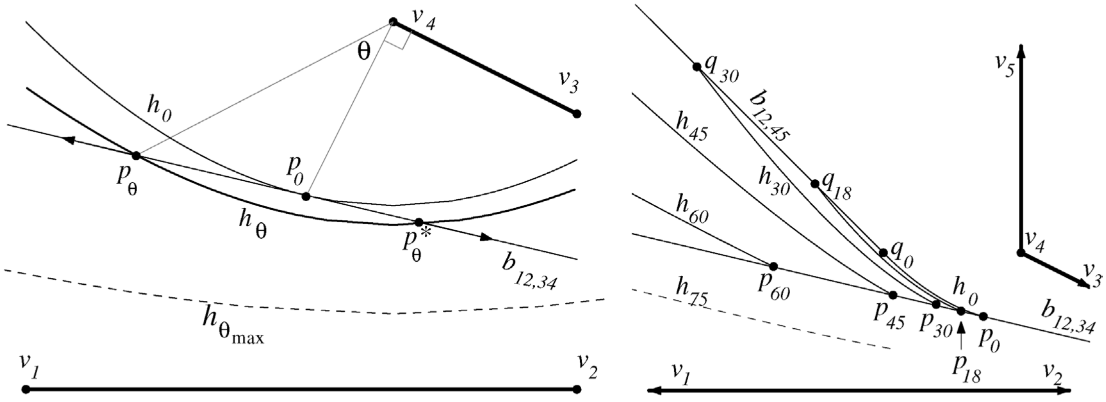

Fig. 8. (Left) Illustration of the connection of a hyperbolic (vertex–edge) bisector with the appropriate edge–edge bisector at its centrifugal end in forming the DA for $\theta > 0$. (Right) Illustration of the connection of a hyperbolic bisector at both (centrifugal and centripetal) ends.

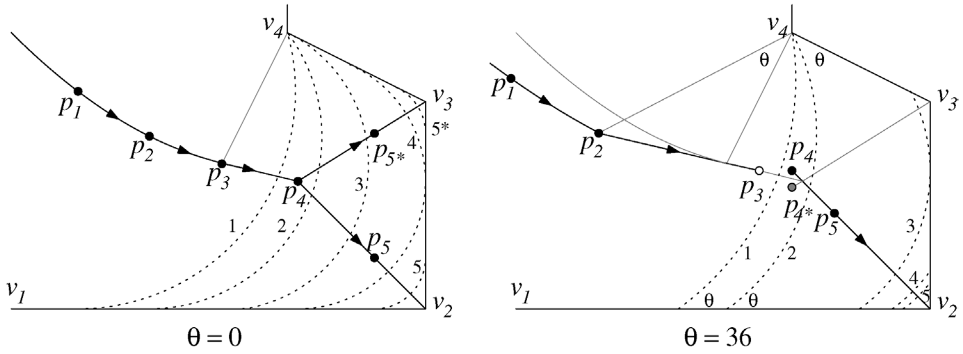

θ = 0

θ = 36

Fig. 9. Comparison of MA (left) and DA (right) (dark solid lines) in the $v_1 \to v_4$ region of a given polygon. Dotted curves show drainage menisci configurations. Menisci i has its center of curvature at point p_i.

one point (the incorrect point p_θ^*). The $p_{\theta_{\max}}$ branch of the hyperbolic bisector becomes asymptotic to $b_{12,34}$. Let $2\beta_{\text{eff}}$ denote the effective angle between edges v_1v_2 and v_3v_4. Then $\theta_{\max} = \pi/2 - \beta_{\text{eff}}$, i.e. $\theta_{\max}$ is exactly the wetting angle at which the effective vertex formed by edges v_1v_2 and v_3v_4 will not support a meniscus. For $\theta > \theta_{\max}$ the DA will not extend into the $v_1 \to v_4$ vertex region. Thus the DA construction naturally determines which "effective" corners of the polygon will support arc menisci for any prescribed wetting angle.

The illustration on the right in Fig. 8 also includes an edge v_4v_5 in order to illustrate connection of the hyperbolic bisectors at both ends. In this illustration, proceeding centrifugally from the polygon interior, for $0 \leqslant \theta < 45°$ the DA will consist locally of: a segment of the $b_{12,45}$ bisector to the point q_θ; a segment of the h_θ hyperbolic bisector from q_θ to p_θ; and then a segment of the $b_{12,34}$ bisector. The hyperbolic bisector h_{45} is centripetally asymptotic to $b_{12,45}$ (but not to $b_{12,34}$); thus for $45° \leqslant \theta < \theta_{\max}$ the DA consists locally of the h_θ hyperbolic bisector to p_θ at which point it connects to the $b_{12,34}$ bisector. (Specification of the rest of the polygon perimeter is required to describe how the hyperbolic bisectors in this angular range connect with the rest of the DA.) Finally, as discussed for the left figure, for $\theta > \theta_{\max}$, no DA branch is associated with the $v_1 \to v_5$ "corner" of this polygon, as this corner will not support a meniscus. For this example, $\theta_{\max} \approx 73.15°$. The $\theta = 75°$ bisector, h_{75}, is shown as a dashed line in the figure.

Let p be the center of curvature of an arc meniscus. p lies on a bisector of two perimeter components, $\mathcal{C}_1$ and $\mathcal{C}_2$; thus the two ends of the meniscus terminate on $\mathcal{C}_1$ and $\mathcal{C}_2$ with the appropriate wetting angle, θ. Assume this meniscus tangentially touches a third, distinct, perimeter edge $\mathcal{C}_3$. We refer to such bisector points p as *edge-contact points*. For $\theta = 0$, edge contact points are branch points of the MA tree and correspond to points that are common to more than one bisector. If $\theta = 0$, a meniscus having center of curvature at an edge contact point is stable, but the meniscus will split under infinitesimal increase in capillary pressure. For $\theta > 0$, the menisci corresponding to edge contact points are unstable, as they contact the edge $\mathcal{C}_3$ at the wrong angle; such menisci must spontaneously undergo a change in topology (with no change in capillary pressure). These edge contact points are again branch points of the DA but, in general, they no longer correspond to points common to more than one bisector.

The situation is illustrated in Fig. 9. For $\theta = 0$, the depicted MA consists of a parabolic bisector (associated with perimeter vertex v_4 and edge v_1v_2), and three edge–edge bisectors (associated with edge-pairs v_1v_2–v_3v_4, v_1v_2–v_2v_3, and v_2v_3–v_3v_4). Point p_4 is an edge contact point, forming the MA branch point joining the three edge–edge bisectors. The stable meniscus labeled 4, centered at p_4 is tangential to edges v_1v_2, v_2v_3, and v_3v_4.

For a DA, (Fig. 9, right), the parabolic bisector is replaced by a hyperbolic bisector, which joins the v_1v_2–v_3v_4 edge–edge bisector at the point p_2. Point p_3 on this edge–edge bisector is an edge contact point, as can be seen from its associated meniscus (labeled 3). Thus no part of the v_1v_2–v_3v_4 edge–edge bisector centrifugal to point p_3 can be part of the DA. Instead the DA continues at the point p_4 on the v_1v_2–v_2v_3 edge–edge bisector. Point p_4 has the property that $r(p_4) = r(p_3)$; it is easily found since the line segment p_3, p_4 must be parallel to the edge v_1v_2. When the meniscus center of curvature reaches p_3, its meniscus (labeled 3) becomes unstable, and the center jumps discontinuously to p_4 where a stable meniscus (labeled 4) of the same radius of curvature forms. Although the DA is spatially discontinuous from p_3 to p_4 the DA is still conceptually a tree, providing we identify the points p_3 and p_4 as a common branch point of the tree. This identification of spatially separated points as forming a common branch point of the DA tree is consistent since the radius function $r(p)$ is continuous at these identified points.

For the particular geometry shown in Fig. 9, with $\theta = 36°$, $\beta(v_3) + \theta > \pi/2$ and no meniscus can exist in corner v_3. However, for $\theta < \pi/2 - \beta(v_3)$, the DA will also have a branch continuing on the v_2v_3–v_3v_4 edge–edge bisector. This continuation would occur at the point p_{4^*} which also has the property that $r(p_{4^*}) = r(p_3)$. Again, p_{4^*} is easily found as the line segment p_3, p_{4^*} must be parallel to the edge v_3v_4. In such a case, the unstable meniscus 3 would split into two stable meniscus of the same radius of curvature centered at p_4 and p_4^*. Interpretation of the DA as a tree requires identifying the points p_3, p_4, and p_{4^*} as forming a common branch point. It also requires recognizing that the one spatial point which is common to both the v_1v_2–v_2v_3 and v_2v_3–v_3v_4 bisectors, which does form a branch

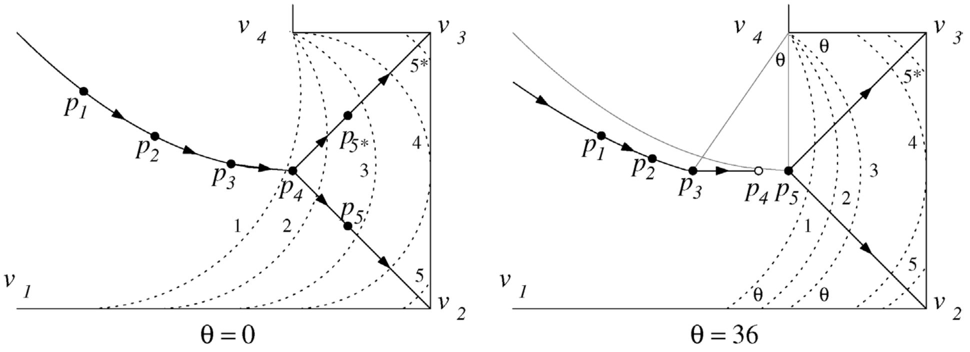

Fig. 10. Comparison of MA (left) and DA(30) (right) in the $v_1 \to v_4$ region of a given polygon. Dotted curves show drainage menisci configurations. Menisci i has its center of curvature at point p_i.

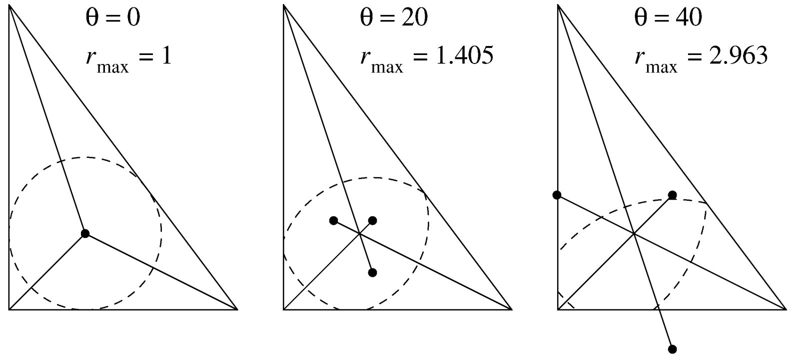

Fig. 11. MA and DAs (solid lines) for a triangular polygon showing splitting and movement, as a function of θ, of the points identified in common as the root of the DA tree.

point in the MA, is no longer to be identified as common to the two bisectors in the case of the DA.

The discussion of Fig. 9 demonstrates that segments of edge–edge (and vertex–vertex) bisectors appearing in the DA are generally longer than the segments of the same edge–edge bisector appearing in the MA. One notable example of this is the case of edge–edge bisectors segments which are present only in a degenerate (zero-length) sense in the MA, and appear as finite length segments in the DA. This is illustrated in Fig. 10. In the MA (Fig. 10 (left)), the parabolic v_4–v_1v_2 vertex–edge bisector joins the two (v_1v_2–v_2v_3 and v_2v_3–v_3v_4) edge–edge bisectors at point p_4. There is no v_1v_2–v_3v_4 edge–edge bisector in the MA, though it can conceptually be said to be represented as a zero-length segment at point p_4 (since p_4 is indeed on the v_1v_2–v_3v_4 edge–edge bisector). However, for $\theta > 0$, as illustrated in Fig. 10 (right), this bisector appears as a segment of non-zero length to connect the hyperbolic bisector to the v_1v_2–v_2v_3 and v_2v_3–v_3v_4 edge–edge bisectors. As per discussion on Fig. 9, the DA is spatially discontinuous at the edge contact point p_4 which is to be identified with the point p_5, the continuation point of the DA in the centrifugal direction. (As edges v_1v_2 and v_3v_4 are parallel in this example, no extensions of the v_1v_2–v_2v_3 and v_2v_3–v_3v_4 edge–edge bisectors occur.)

We note that these edge–edge segment extensions always occur in the centripetal direction on the DA.

The discussion of Figs. 9 and 10, which demonstrates (centripetal) extensions of edge–edge segments and resulting spatial discontinuity in the branch points of the DA tree, has implications for the root of the DA tree. In Fig. 11, we illustrate this for a simple triangular polygon. The left figure in Fig. 11 shows the MA tree (solid line), the root of the tree (dark point) and the maximally inscribed circle (MIC) (dashed line) centered at the root. The radius of this MIC represents the largest possible radius of curvature achievable by any meniscus involving a perfectly wetting fluid; it is therefore appropriate to view the MIC as the union of three maximal radius menisci. (For any polygon, it is the property of the MA, equivalently the property of perfectly wetting fluids, that the corresponding maximal radius menisci meet as a perfect circle centered at the root the MA.)

For $\theta > 0$, the largest radius meniscus that can be associated with a DA leaf-to-root path is limited by its intersection with some meniscus (of the same radius) associated with a different leaf-to-root path. For triangles, the largest meniscus radius possible occurs when the three corner menisci (of that radius) at most touch but do not overlap. As demonstrated in Fig. 11 for $\theta = 20°$ and 40°, for triangles this generally occurs when two of the menisci touch (along their common edge) and the third meniscus touches neither. (For triangles, no larger radius meniscus would be stable.) If the three points which define the centers of curvature of these maximal radius meniscus are identified as forming the root of a tree, we see that the DA is a tree structure. Although, in this example the edge–edge bisectors branching from the root do cross in physical space at the center of mass of the triangle, we again note that this physical crossing is ignored in viewing the DA as a tree structure.

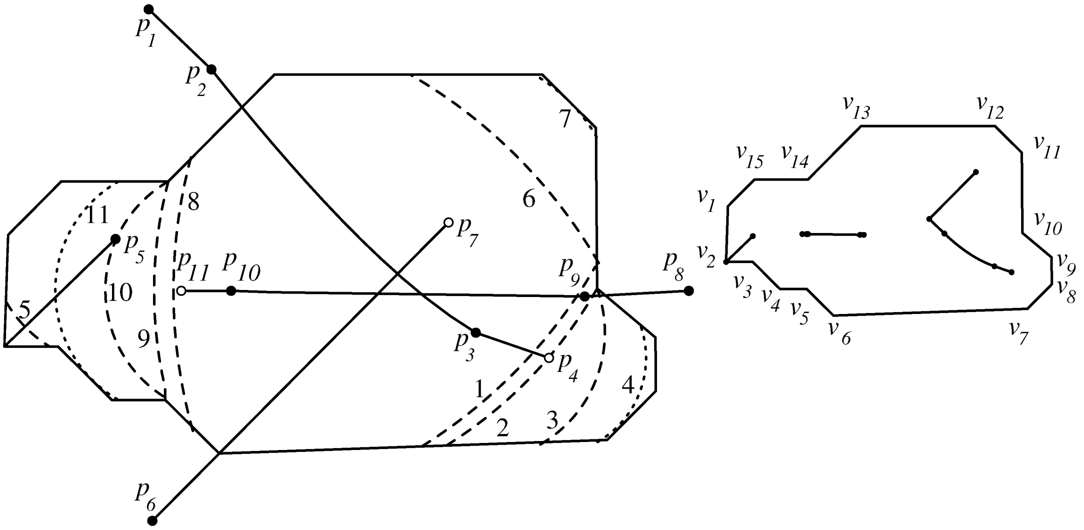

Fig. 12. (Left) DA(30) for the polygon of Fig. 4. (Right) The branches from the MA of Fig. 4 that correspond to branches of the DA in the left figure.

We have, to this point, developed the local structure of a DA which follows from two underlying physical consequences that must hold under increasing values of θ: the centripetal extension of edge–edge bisector segments and the presence of hyperbolic bisectors. The union of the local structures comprise the global DA. Thus by construction:

Theorem 2. *For the displacement of a fluid of intermediate* $(0 < \theta < \pi/2)$ *wettability, the centers of arc-menisci separating the two fluids must lie on the interior DA*(θ) *of the polygon.*

Based upon our local structure analysis, we conjecture the following characterization of the global character of the DA:

With two amendments, properties 0 through 4 remain true for any DA. The amendments are that the DA tree structure is generally discontinuous in physical space at branch points of the tree, including the root, and that a leaf vertex of the tree may no longer be coincident with a vertex location on the polygon perimeter.

Support for this conjecture awaits the completion of a numerical algorithm (designed under these local structure construction principles) to compute the DA and resultant meniscus positions under primary drainage for comparison with experimental results.

We note that there are interesting theoretical questions in computational geometry concerning the DA for simply connected polygons. Two of these are: can any DA be constructed in linear time, and is every DA related to a Voronoi-like tessellation of the polygon interior? We believe the answer to the first of these questions is yes.

3.1. *Entry pressure meniscus configuration*

If, as conjectured, properties $0 \to 4$ also hold for the DA, and Assumption 1 is invoked, then a unique solution of (6) on the DA constructed for any given angle θ can be obtained using the same bisection search algorithm designed for the MA. Although we have not completed a numerical construction algorithm for DAs, Fig. 12 (left) shows hand computation of the DA(30) for the polygon in Fig. 4. The bisector segments comprising the DA are displayed as solid curves. Labeled points indicate branch points of the DA where bisector segments change type or terminate. The menisci (broken curves) corresponding to the labeled points are also shown. Menisci drawn as dashed curves are stable. Menisci 1, 6, 8 represent the largest radius menisci possible; the corresponding points p_1, p_6 and p_8 are identified in common as the root of the DA tree. Menisci 4, 7, 11 (drawn as dotted curves) are unstable, their corresponding centers of curvature p_4, p_7, p_{11} (open points) are edge contact points. Point p_5 is the stable counterpart to p_{11}; these two points are identified in common as a branch point of the DA; the radius of curvature of their corresponding menisci, 5 and 11, are identical. When a meniscus center of curvature reaches p_{11}, there is an immediate topological change in the meniscus (from 11 to 5) with no change in radius as the center point shifts from p_{11} to p_5. Note that the edge contact point p_4 has no stable counterpart; when the meniscus center reaches p_4 the meniscus 4 breaks up and the entire $v_7 \to v_{10}$ corner of the polygon interior is filled with non-wetting fluid. A similar statement follows for the edge contact point p_7.

The right figure in Fig. 12 isolates the bisector segments of the MA that correspond to those in DA(30). Note that for $\theta = 30°$, out of the 15 vertices comprising the polygon perimeter, only vertex 2 is capable of supporting a meniscus. However, menisci are supportable by "effective" vertices formed by combinations of polygon components—these component pairs correspond with bisector segments of the DA. *It is important to note that it is not solely the angle between a pair of perimeter edge components that determines whether the pair will support a meniscus.* In the polygon of Fig. 12, the edge pair v_7v_8–v_9v_{10} defines an effective angle that would, by itself, support a meniscus between them when $\theta = 30°$. However, the placement of the edge v_8v_9 eliminates any possibility of a physical meniscus between v_7v_8 and v_9v_{10}. The edge pair, v_6v_7–v_9v_{10} does support a meniscus, but only until the edge contact point p_4 on its corresponding bisector is reached. At this point the menis-

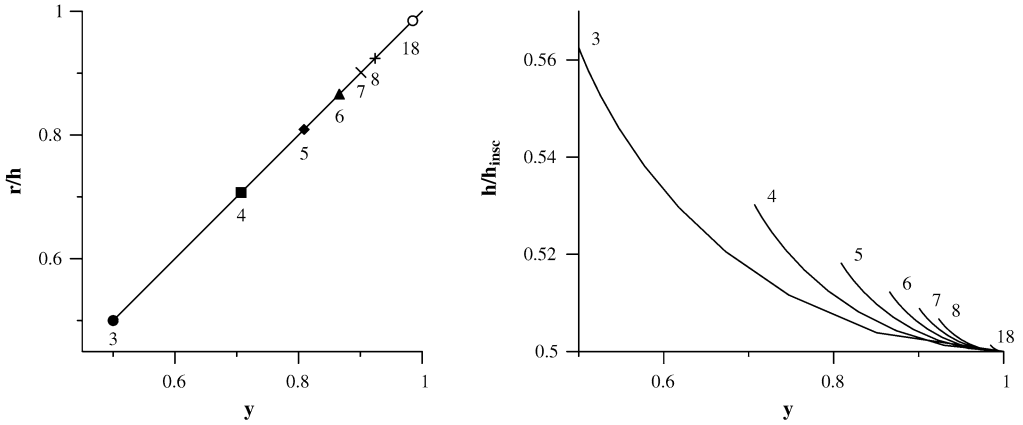

Fig. 13. The behavior of r/h and h/h_{insc} as a function of the scaling variable y for regular convex polygons on n vertices. In the left plot, the labeled points indicate the values $\cos(\pi/n)$.

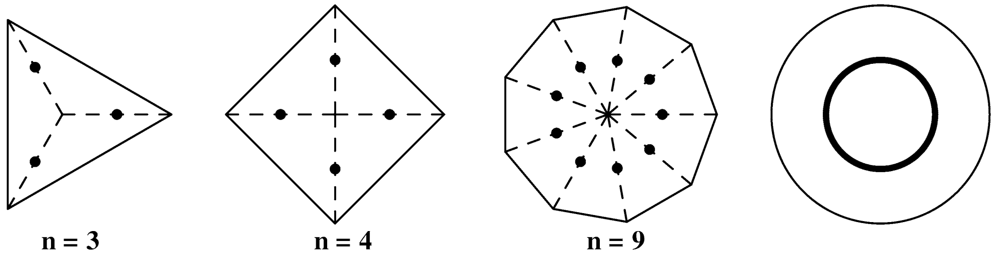

Fig. 14. (Left three figures) Limiting position (points) of the centers of curvature for arc menisci for regular convex polygons at the critical wetting angle $\theta = \pi/n$ at which the menisci vanish (corners are filled with non-wetting fluid). Considering the circle as the $n \to \infty$ limit of regular convex polygons, the limiting position of the center of curvature of any meniscus falls on the dark circle, and the limiting value of the radius of curvature is $r_{\text{circ}}/2$.

cus (labeled 4) becomes unstable, and the *entire* effective vertex $v_6 \to v_{10}$ becomes filled by the non-wetting fluid.

3.2. *Over-pressure in primary drainage, $\theta > 0$*

Under over-pressurization, our conjectures on the properties of the global structure of the DA imply that meniscus centers will move in the centrifugal direction. When a meniscus center hits a contact point, a new feature appears: the center and its corresponding menisci will jump discontinuously in space, possibly accompanied by a split in the meniscus, with *no change* in radius of curvature. This was illustrated by the transitions $p_3 \to p_4$ and $p_4 \to p_5$ in the right hand side figures of Figs. 9 and 10, respectively.

4. Regular convex polygons

Although we can now compute the position of the arc menisci for $\theta = 0$ for any polygon (Section 5 presents results for entry pressure configurations), we have not currently constructed numerical algorithms to generate the DA and solve (6) for $\theta > 0$. We can however construct the DA for any regular convex polygon (or irregular triangle), although the construction is unnecessary as the regular nature of their DA allows for analytic solution (12). The analytic solution for regular convex polygons were extensively studied by Ma et al. [19]. We would like to add one observation for regular convex polygons derived from addressing the question: what is the position and radius of the arc menisci as θ approaches the limiting case $\theta \to \pi/2 - \beta$, where β is the half-angle common to all vertices in a regular polygon?

Let h_{insc} denote the distance from any vertex to the center of mass of a regular convex polygon. Let h be as defined in Fig. 2. We are interested in the behaviors of r and h as $\theta \to \pi/n$ for any regular convex polygon of n vertices. From (12) the behavior can be represented in terms of a scaling variable

$$y \equiv \cos(\pi/n)/\cos\theta, \qquad y \in \big[\cos(\pi/n), 1\big]. \tag{13}$$

As shown in Fig. 13 (left), r/h has universal behavior

$$r/h = y, \qquad y \in \big[\cos(\pi/n), 1\big] \tag{14}$$

as θ increases from 0 to π/n. Thus $r = h$ at the critical value of wetting angle $\theta = \pi/n$. The behavior of h/h_{insc} is shown on the right of Fig. 13. We note, $h < h_{\text{insc}}$ for all allowed values of θ, and h falls monotonically to $h_{\text{insc}}/2$ as $\theta \to \pi/n$. Thus, the meniscus configuration disappears (all vertices filled with non-wetting fluid) for any regular convex polygon when $\theta = \pi/n$. *Furthermore, the menisci disappear by becoming exactly coincident with the vertices of the polygon at a finite radius of curvature value of $h_{\text{insc}}/2$.* This is illustrated in the left three figures in Fig. 14. As $h_{\text{insc}} = r_{\text{mic}}/\cos(\pi/n)$, this generates the result $P_C^e(\theta = \pi/n) = 2\sigma\cos(\theta)/r_{\text{mic}}$, in agreement with Eqs. (3) and (22) in [19].

This mechanism of meniscus disappearance at a critical wetting angle explains a familiar result under the limit $n \to \infty$ (where a regular convex polygon approaches a circle). As

$n \to \infty$, $h_{\text{insc}} \to r_{\text{circ}}$, where r_{circ} is the radius of the circle. *Thus for a circular cross section, for any value of* θ*, the meniscus configuration becomes coincident with the perimeter of the circle* (*zero width wetting film*)*, the radius of curvature of the arc menisci is* $r = h_{\text{insc}}/2 = r_{\text{circ}}/2$*, and the centers of curvature of the menisci lie on a concentric circle of radius* $r_{\text{circ}}/2$, as shown in Fig. 14 (right). The consequence of this is the familiar entry pressure condition for a cylinder,

$$P_C^e = 2\sigma/r_{\text{circ}}. \tag{15}$$

Viewing a circle as a limiting case of regular polygons thus explains geometrically why the factor $r_{\text{circ}}/2$ appears in (15).

5. Entry pressures for throats in Fontainebleau sandstone, $\theta = 0$

CT now provides three-dimensional images of rock and soil samples [33,34] at voxel resolutions below 5 µm. Algorithms, and in some cases, complete software packages have been developed to analyze the geometry of the pore structure [25,35,36] from such images. In [25] we characterized the throats by area and effective radius for a suite of four Fontainebleau sandstone core sample ranging from 7.5 to 22% porosity. These sandstones were imaged at 5.7-µm resolution. Here we consider the full polygonal representation of each throat as deduced from the CT images.

Polygonal representations of throats in the imaged core samples were obtained using the 3DMA-rock software package (http://www.ams.sunysb.edu/~lindquis/3dma/3dma_rock/3dma_rock.html). A discussion of the throat finding algorithm used for this data set is found in Lindquist and Venkatarangan [35]. The salient points are that the throat is characterized by (i) a closed loop of 26 connected grain voxels which form the perimeter of the throat; (ii) a void space voxel which characterizes the location of the throat along the channel centerline in which the throat is located; (iii) a triangulated surface (using the voxels from (i) and (ii) from which the area of the throat is computed. These digitized throats characterize the location of minimum cross section area in the channel, but our algorithms do not enforce a requirement that the throats are planar. Thus the throats minimize cross-sectional area by following the cross-sectional geometry of the channel.

As the discussion in Sections 2 and 3 implicitly assumes the polygons analyzed are planar, we project each digitized throat onto a plane that is perpendicular to the (average) normal to the throat surface (see (iii) above). The projection of the center point of each throat perimeter voxel provides the vertex coordinates of the (projected) perimeter polygon. As deviation from planarity is rather mild for the vast majority of throats, this projection introduces no significant artifact. (In fact, of the over 21,500 throats analyzed in this study, less than 10 had a projection artifact which caused the analysis to fail. In all cases the artifact was a projected perimeter that self intersected at a single point—i.e. the projected polygon was not simply connected.) For the remainder of the discussion we shall drop the reference to "projected" and refer simply to the throat polygons.

The MA for the interior of each throat polygon was computed using Held's Vroni software package [31] (http://www.cosy.sbg.ac.at/~held/projects/vroni/vroni.html) which is noteworthy for its speed and robustness. Vroni was modified by adding a bisection algorithm to compute the solution to (6). The accuracy of the numerical solution was verified using the $\theta = 0$, analytic results (12) for regular polygons. Comparing numerical and analytic values for the dimensionless ratio $(A/P)/r_e$, the numerical solution for r_e was determined to be accurate to three significant digits.

Fig. 15 shows solutions of (6) by displaying the entry pressure meniscus positions (solid arcs), and meniscus center positions (solid points) for the first 16 of the 9294 throats analyzed in the 22% porosity Fontainebleau sample. (For the sake of brevity, we do not show results for the other three porosity samples. The results from these other three are completely consistent with those reported here for the 22% porosity sample.) The throats are not drawn to mutual scale; the relative sizes of each throat can be deduced by noting that the smallest edge length in each polygon perimeter must be of the size of a single voxel. (Thus the lower left throat in Fig. 15 is rather large.) Also displayed for each throat is the MA (tree structure of gray line segments) and the largest MIC (dashed curve) for the polygon which is centered on the MA vertex which serves as the root (larger open circle) of the MA tree.

Having highly accurate results for r_e, we address the question of various methods of approximation for the entry pressure P_C^e, or equivalently, for approximation of r_{e}. We consider three methods: (i) the Haines approximation [37] $r_e \approx r_{\text{mic}}$, where r_{mic} is the largest inscribable radius in the throat; (ii) $r_e \approx r_{\text{area}} \equiv \sqrt{A/\pi}$, where A is the throat area; (iii) Hwang's [38] hydraulic radius approximation, $r_e \approx A/P = GP$, where P is the throat perimeter and G the shape factor. Distributions for r_{e}, r_{mic} r_{area} and A/P determined for the 9294 throats found in the 22% porosity Fontainebleau sample are shown in Fig. 16. Also shown are distributions for the ratios $r_{\text{mic}}/r_{\text{e}}$, $r_{\text{area}}/r_{\text{e}}$, $(A/P)/r_{\text{e}}$. Both r_{mic} and r_{area} overestimate r_e by factors of 1.5 → 2.0 and 2.0 → 3.0, respectively. Though A/P slightly underestimates r_{e}, *Hwang's hydraulic radius approximation is a very good estimator of the entry meniscus radius for real throats in Fontainebleau sandstone for* $\theta = 0$. The A/P versus r_{e} scatterplot shown in Fig. 16 emphasizes the quality of the estimation. As mentioned, identical conclusions are found for the other three porosity samples analyzed. The accuracy of A/P as a predictor for r_{e} can be compared against the known analytic result (12) for values of n and θ restricted by (9). The resulting plot of $(A/P)/r_{\text{e}}$ versus n for the significant range of θ is shown in Fig. 17. (Missing is the $\theta = 60$ degree plot, which has a single allowed value, $(A/P)/r_{\text{e}} = 0.5$ for $n = 3$.) $(A/P)/r_{\text{e}}$ is a monotonically increasing function of n. For wetting angles 10° and below, the $(A/P)/r_{\text{e}}$ ratio lies between 0.88 and 1.0. This is consistent with our $\theta = 0$ results for Fontainebleau throats where we find an average value for $(A/P)/r_{\text{e}}$ of 0.96 ± 0.03 (Fig. 16).

There is, of course, a question of the effect of finite voxel resolution on the accuracy of the results computed for real sandstones. As polygon shape is determined by vertex locations, fi-

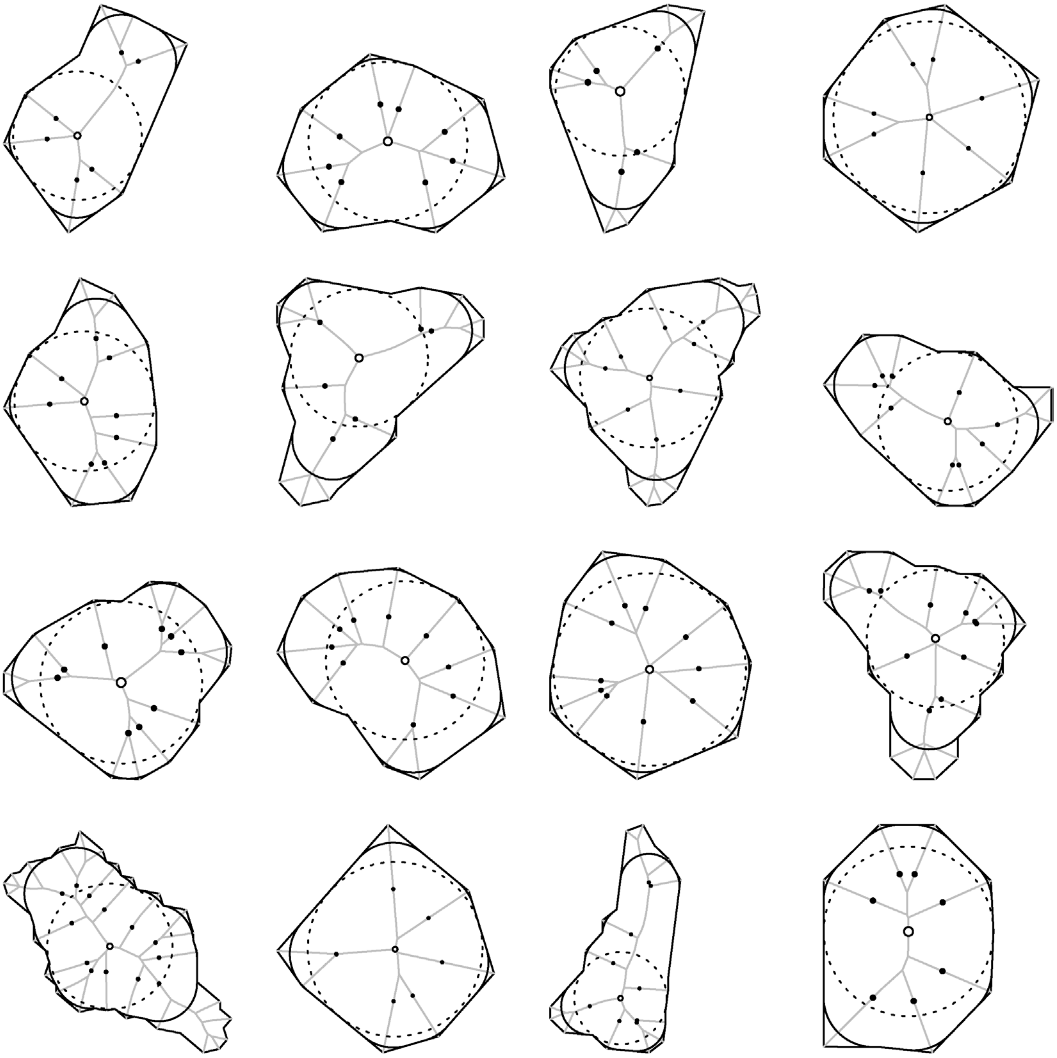

Fig. 15. Arc meniscus locations (solid arcs) at entry pressure for $\theta = 0$ for the first 16 (of 9294) throats analyzed in the 22% porosity Fontainebleau core sample image. Solid points indicate centers of curvature of the menisci. The dashed circle is the maximally inscribed circle, centered at the root location (open point) of the MA (solid gray lines).

nite voxel resolution can affect accuracy through "corner rounding" and "loss of sharp points." Our experience with CT imaging of sandstones, which leads us to conclude that effects due to rounding will be small, can be quantified somewhat by noting that the grains in Fontainebleau (which has a well sorted grain size distribution) have diameters in the 200–250 μm range. Thus grain perimeters are resolved quite well. Corner rounding will produce minor deviations from true meniscus configuration, for example at high overpressure values when menisci are forced deep into corners.

6. Summary

We have shown that, at entry pressure and higher, during primary drainage, away from the main terminal meniscus, the arc meniscus configuration in a capillary tube whose cross section is that of an arbitrary, simply connected polygon, can be determined from an analysis of the drainage axis computed on the polygon interior for the specified wetting angle governing the two-fluid displacement process. In the case of zero wetting angle (displacement of a perfectly wetting fluid) the drainage axis is the familiar medial axis of the polygon interior. As the centers of curvature of all menisci must remain on the drainage axis during primary drainage. the geometry of the drainage axis explains and predicts, in full detail, the topological changes, pinning behavior, and discontinuous movement of menisci during primary drainage. It also predicts at what pressure any "corner" of the capillary tube will become completely invaded by the non-wetting fluid.

We present details for constructing the drainage axis and an algorithm for solving for the entry pressure meniscus configuration. Using existing software for medial axis construction, we compute the entry pressure radii for over 21,500 polygonal throats determined from analysis of 4 samples of Fontainebleau sandstone. Our results demonstrate that Hwang's hydraulic radius approximation is an excellent predictor for the entry pressure meniscus radius for real throats. We expect the accuracy of Hwang's approximation to lessen for non-zero wetting angles.

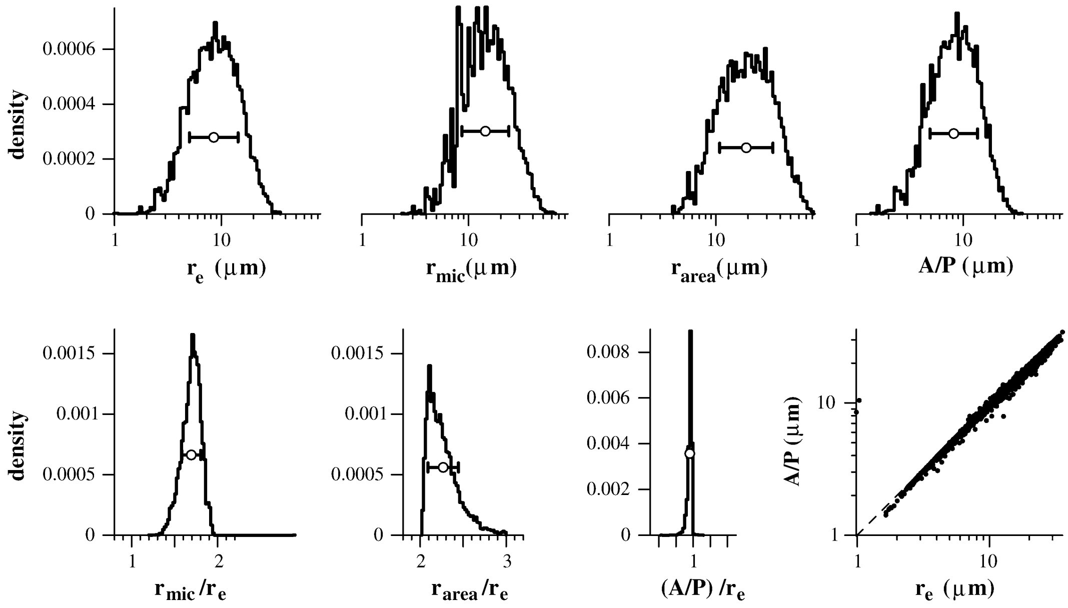

Fig. 16. Measured distributions for r_e, r_{mic}, r_{area}, A/P, and ratios of these last three with the true meniscus entry pressure radius r_e from analysis of the throats in the 22% porosity Fontainebleau sandstone sample. Mean and standard deviations for each distribution are given by open points/horizontal whiskers. The bottom right plot, a scatter plot of A/P versus r_e, emphases the predictive nature of A/P for r_e.

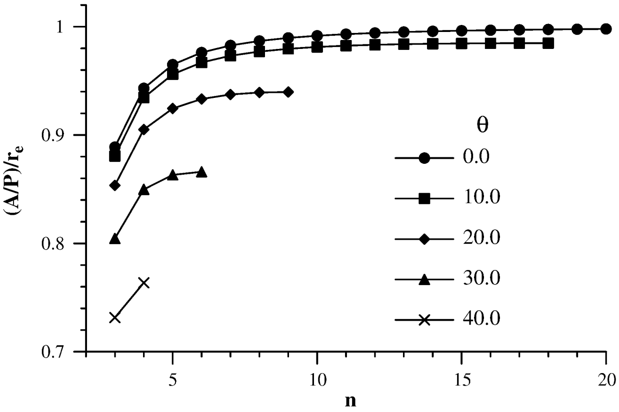

Fig. 17. Plot of $(A/P)/r_e$ as a function of n and θ from (12) for regular, n-sided, polygons.

The extent of this weakening awaits completion of a numerical algorithm for construction of DAs.

The geometry presented here governs the shape of the meniscus "far removed" from the terminal meniscus. Ultimately it must be related to three-dimensional capillary shape (e.g. [39]). It is tempting to conjecture that, for polygonal capillaries, in any cross section perpendicular to the capillary axis the arc menisci remain centered on the drainage axis (of the cross section) regardless of how close the cross section is to the tip of the terminal meniscus. If this conjecture is true, this may provide a technique for surface shape solutions of the capillary equation [40] to compete with finite element based techniques [41].

Acknowledgments

This work was supported by the U.S. Department of Energy, Grant DE-FG0205-ER-15635. The author is indebted to Martin Held (University of Salzburg) for access to his Vroni software, and to Joseph Mitchell (Stony Brook University) for many discussions on medial axis analysis.

References

[1] R.P. Mayer, R.A. Stowe, J. Colloid Interface Sci. 20 (1965) 893.
[2] H.M. Princen, J. Colloid Interface Sci. 34 (1970) 171.
[3] T.W. Patzek, SPE J. 6 (2001) 144.
[4] M.J. Blunt, Curr. Opin. Colloid Interface Sci. 6 (2001) 197.
[5] M.I.J. van Dijke, K.S. Sorbie, J. Colloid Interface Sci. 260 (2003) 385.
[6] R. Lenormand, C. Zarcone, A. Sarr, J. Fluid Mech. 135 (1983) 337.
[7] H.M. Princen, J. Colloid Interface Sci. 30 (1968) 69.
[8] H.M. Princen, J. Colloid Interface Sci. 30 (1969) 359.
[9] F.M. Orr Jr., L.E. Scriven, A.P. Rivas, J. Colloid Interface Sci. 52 (1975) 602.
[10] J.A. Dodds, Powder Technol. 20 (1978) 61.
[11] B. Legait, J. Colloid Interface Sci. 96 (1983) 23.
[12] G. Mason, M.D. Nguyen, N.R. Morrow, J. Colloid Interface Sci. 95 (1983) 494.
[13] G. Mason, N.R. Morrow, J. Colloid Interface Sci. 100 (1984) 519.
[14] G. Mason, N.R. Morrow, J. Colloid Interface Sci. 109 (1986) 46.
[15] G. Mason, N.R. Morrow, J. Colloid Interface Sci. 141 (1991) 262.
[16] P.-E. Øren, S. Bakke, O.J. Arntzen, SPE J. 3 (1998) 324.
[17] M. Lago, M. Araujo, J. Colloid Interface Sci. 243 (2001) 219.
[18] G. Mason, N.R. Morrow, J. Chem. Soc. Faraday Trans. 80 (1984) 2375.
[19] S. Ma, G. Mason, N.R. Morrow, Colloids Surf. A 117 (1996) 273.
[20] D. Langbein, Springer Tracts Modern Phys. 178 (2002) 179–211.
[21] M.J. Blunt, M.D. Jackson, M. Piri, P.H. Valvatne, Adv. Water Resour. 25 (2002) 1069.
[22] H.W. Deckman, J.H. Dunsmuir, K.L. D'Amico, S.R. Ferguson, B.P. Flannery, Proc. Mater. Res. Soc. Symp. 217 (1991) 97.
[23] J.F. Thovert, J. Salles, P.M. Adler, J. Microsc. Oxford 170 (1993) 65.
[24] Z. Liang, M.A. Ioannidis, I. Chatzis, J. Colloid Interface Sci. 221 (2000) 13.
[25] W.B. Lindquist, A. Venkatarangan, J.H. Dunsmuir, T.-F. Wong, J. Geophys. Res. 105 (2000) 21508.
[26] D.B. Silin, G.D. Jin, T.W. Patzek, J. Petrol. Tech. 56 (2004) 69.

[27] H. Shin, W.B. Lindquist, D.L. Sahagian, S.-R. Song, Comput. Geosci. 31 (2005) 473.
[28] P. Concus, R. Finn, Proc. Nat. Acad. Sci. USA 63 (1969) 292.
[29] A. Rosenfeld, Comput. Vision Graph. Image Process. 33 (1986) 156.
[30] R. Ogniewicz, M. Ilg, in: Proc. IEEE Comput. Soc. Conf. Comput. Vision Pattern Recog, Champaign, Il, June 1992, pp. 63–69.
[31] M. Held, Comput. Geom. Theory Applic. 18 (2001) 95.
[32] E.W. Weisstein, "Conic Section." From MathWorld—A Wolfram Web Resource. http://mathworld.wolfram.com/ConicSection.html.
[33] P. Spanne, J.F. Thovert, C.J. Jacquin, W.B. Lindquist, K.W. Jones, P.M. Adler, Phys. Rev. Lett. 73 (1994) 2001.
[34] D. Wildenschild, J.W. Hopmans, C.M.P. Vaz, M.L. Rivers, D. Rikard, B.S.B. Christensen, J. Hydrol. 267 (2002) 285.
[35] W.B. Lindquist, A. Venkatarangan, Phys. Chem. Earth 25 (1999) 593.
[36] W.B. Lindquist, in: U. Bonse (Ed.), Developments in X-Ray Tomography III, in: Proc. SPIE, vol. 4503, SPIE, Bellingham, WA, 2002, p. 103.
[37] W.B. Haines, J. Agr. Sci. 17 (1927) 264.
[38] S.K. Hwang, Z. Physik. Chemie Neue Folge 105 (1977) 225.
[39] H. Wong, S. Morris, C.J. Radke, J. Colloid Interface Sci. 148 (1992) 317.
[40] D. Langbein, Springer Tracts Modern Phys. 178 (2002) 41–65.
[41] F. M Orr, R.A. Brown, L.E. Scriven, J. Colloid Interface Sci. 60 (1977) 137.